CHAPTER IV
RESULTS AND DISCUSSION

4.1 General Characteristics of API Separator Sludge

The as-received API sludge sample composes approximately 50 wt% of solid, 41 wt% of water and 9 wt% of free oil. The proximate analysis of the API separator sludge compared with selected sludge is given in Table 4.1.

Table 4.1 Proximate analysis of sewage sludge, oil sludge, and API separator sludge

Proximate Analysis (wt%)[a]	Sewage Sludge, (Inguanzo, 2002)	Sewage Sludge, (Dogru, 2002)	Sewage Sludge, (Shen, 2001)	Oil Sludge, (Chang, 2000a)	API separator Sludge
Volatile matter	57.54	53.50	68.88	N/A	48.10
Ash content	27.97	23.48	15.20	1.88	38.36
Moisture	5.20	11.80	5.00	39.15	2.48
Fixed carbon	9.29	11.21	10.93	N/A	11.06
Combustible [b]	66.83	64.71	79.81	58.97	59.16

[a] Wet basis

[b] Volatile + Fixed carbon

As seen from the table, the API separator sludge has lower volatile matter and higher ash content than the sewage sludge (Inguanzo *et al.*, 2002; Dogru *et al.*, 2002; Shen *et al.*, 2001; Chang *et al.*, 2000a). The difference in both contents certainly attributes to the different pyrolysis behavior to some extent. Compared to the oil sludge (Chang *et al.*, 2000a), the API separator sludge has substantially higher ash content. The API separator sludge heating value is comparable to that of other sludge, except the oil sludge, in Table 4.2.

Table 4.2 Heating values of coal, dry sewage sludge, wet sewage sludge, oil sludge and API separator sludge.

Material	Heating Values ($kJ \cdot kg^{-1}$)	Reference
Coal	14600-26700	Inguanzo *et al.*, 2002
-Anthracite	37000	Tienviboon, 1979
-Bituminous	28000	Tienviboon, 1979
-Lignite	24400	Tienviboon, 1979
Dry sewage sludge	12000-20000	Inguanzo *et al.*, 2002
Wet sewage sludge	1000-3000	Inguanzo *et al.*, 2002
Oil sludge (dry basis)	44860	Chang *et al.*, 2000a
API separator sludge	24805	This work

4.2 Thermal Conversion Behaviors

To understand the thermal conversion behavior under the inert atmosphere or pyrolysis behavior of the API separator sludge, a series of experiments were systematically carried out by means of TGA with 5, 10 and $20°C \cdot min^{-1}$ heating rates. Figure 4.1 shows two principle reactions as distinguished by two distinct mass changes over the temperature range for all heating rates. It was found that the first decomposition or weight loss step is between 77 and 327°C while the other is at ca. 327-530°C. The remaining weights are 60 % and 47 % for the first and second steps. Apparently, only slight difference between the pyrolysis behavior of the sludge at the 5 and $10°C \cdot min^{-1}$ heating rate is observed. One explanation could be that the difference of the heating rates is not large enough to significantly affect the pyrolysis behavior. However, with the $20°C \cdot min^{-1}$ heating rate, the difference in the pyrolysis behavior can be observed. That is the weight loss rate or the pyrolysis rate is low compared to that at 5 and $10°C \cdot min^{-1}$. The results also imply that the heating rates would not affect the amount of the solid product from the pyrolysis of the sludge. It

It was observed that solid present after the pyrolysis is approximately 50 wt% of the original weight, which is consistent with the proximate analysis results.

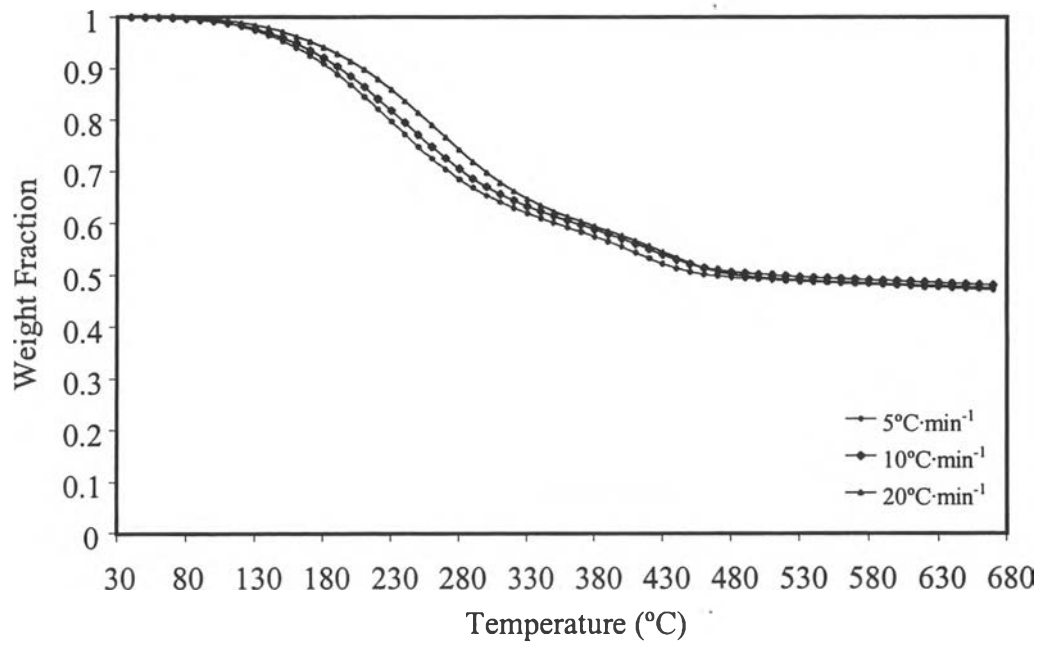

Figure 4.1 Thermogravimetric analysis (TGA) curves of the API separator sludge at various heating rates.

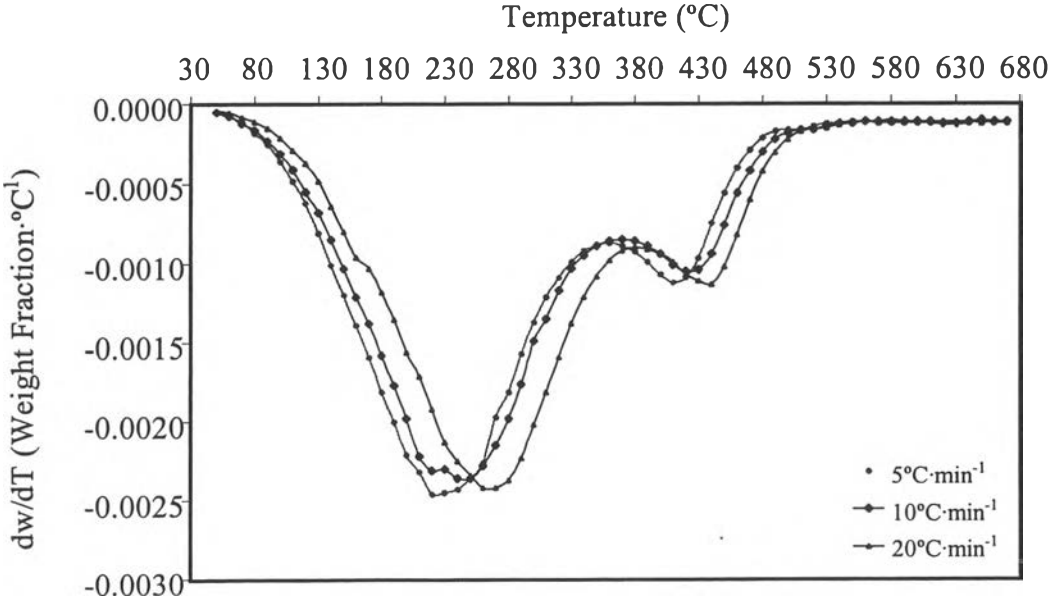

Figure 4.2 Differential thermogravimetric analysis (DTG) curves of the API separator sludge at various heating rates.

The thermal conversion of the sludge can also be viewed from the differential thermogravimetric analysis (DTG) curves, Figure 4.2. Here, two main reactions from the conversion are at 230, 240, and 270; and 415, 430, and 440°C for 5, 10 and 20°C · min^{-1}, respectively. Most of the weight loss takes place at the lower temperatures. Again the high heating rate, 20°C · min^{-1}, has more pronounced effects on the decomposition behavior, especially at the lower temperatures. Comparison with oil sludge (Chang *et al.*, 2000a) shows that the pyrolysis of the API separator sludge has two distinct peaks as mentioned above while the oil sludge has only one board peak with the maximum at 367°C, Table 4.3.

Table 4.3 TGA analysis data of sewage sludge, oil sludge, and API separator sludge

Type	Source	Origin	Maximum Peak Temperature (°C)	Reference
Sludge 1 and Sludge 2	Industrial wastewater plants	Spain	500	Caballero, 1997
Sludge 3	Landfill sample	Altura, (Castellon, Spain)	200, 500	Caballero, 1997
Oil sludge	Crude Oil Storage Tank	The northern, Taiwan	367	Chang, 2000a
API separator sludge	API separator	Rayong, Thailand	230, 415[a] 240, 430[b] 270, 440[c]	This work

[a] Heating rate of 5°C · min^{-1} , [b] Heating rate of 10°C · min^{-1} ,[c] Heating rate of 20°C · min^{-1}

It should also be pointed out that heating rates play a more important role with the pyrolysis of the oil sludge than with the API separator sludge. This may be due to the difference in the amount of ash in both sludges, (see Table 4.1). As the API separator sludge has higher amount of ash, part of the input heat has to go to heat this ash. Consequently, the heating rates do not have so much effect on the sludge. In the contrary, the supplied heat can directly heat up other components in the oil sludge. One can say that the higher amount of ash in sludge, the better heat buffer of the sludge. The thermal conversion behavior of the API separator sludge is more or less the same as that from the industrial wastewater plants (Caballero *et al.*, 1997), Table 4.3. At this point, a full comparison, however, cannot be made because of the incomplete of characterization data of the samples from both sources.

The weight loss of the API separator sludge at the temperature around 250°C is due to volatilization of small components in the sludge such as water, acetic acid, and chloromethane plus the conversion of some small hydrocarbons as indicated by the production of carbon dioxide, Figure 4.3.1-4.3.4 and Table 4.4. An independent experiment was also carried out to substantiate that the weight loss at the low temperature is in fact resulted from the volatilization.

Table 4.4 The possibility identification for mass spectra of light hydrocarbon gases from API separator sludge pyrolysis

m/z	Products
2	H_2 (Hydrogen)
16	CH_4 (Methane)
18	H_2O (Water)
26	C_2H_2 (Acetylene)
42	C_3H_6 (Propene, Cyclopropane)
44	CO_2 (Carbondioxide), CH_3CHO (Acetaldehyde/Ethylene oxide)
50	CH_3Cl (Chloromethane)
56	C_4H_8 (Butene)
60	CH_3CO_2H (Acetic acid)

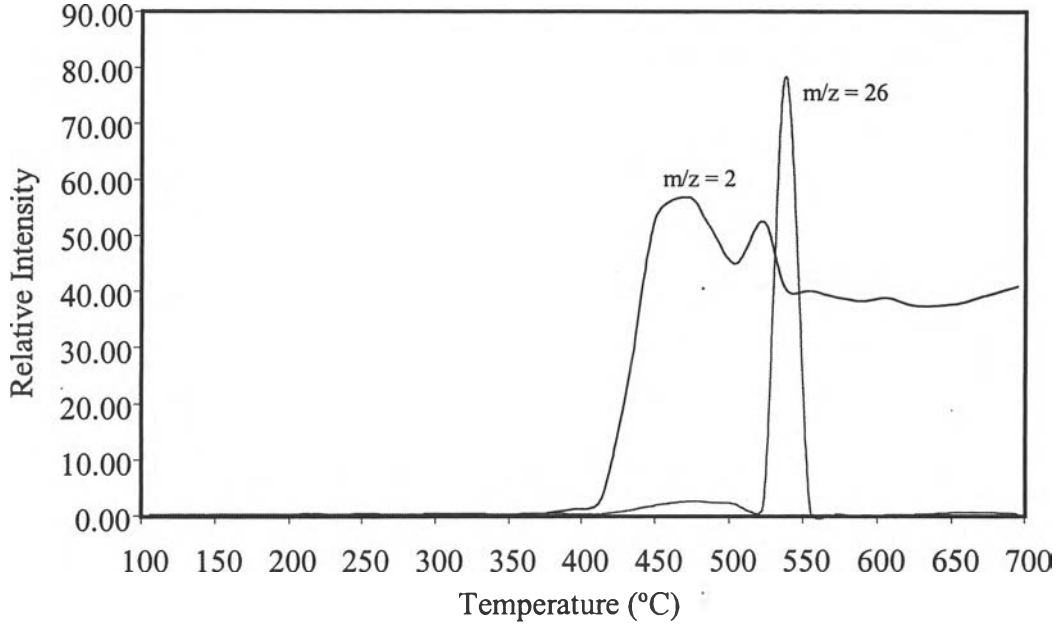

Figure 4.3.1 Mass spectra of products, m/z = 2 and 26, from the pyrolysis of API separator sludge with $10°C \cdot min^{-1}$ heating rate.

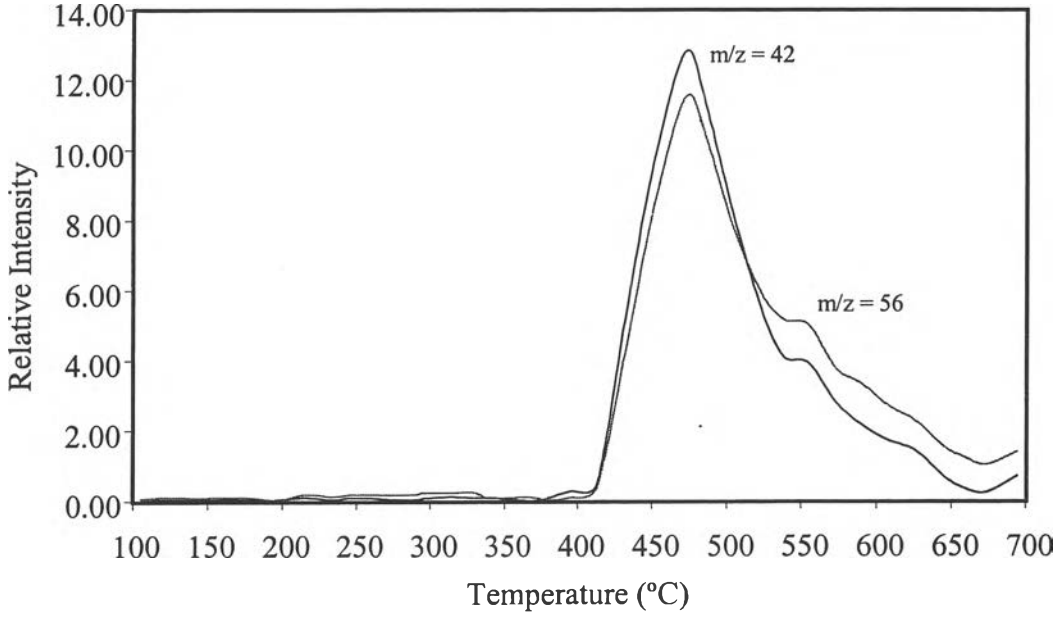

Figure 4.3.2 Mass spectra of products, m/z = 42 and 56, from the pyrolysis of API separator sludge with $10°C \cdot min^{-1}$ heating rate.

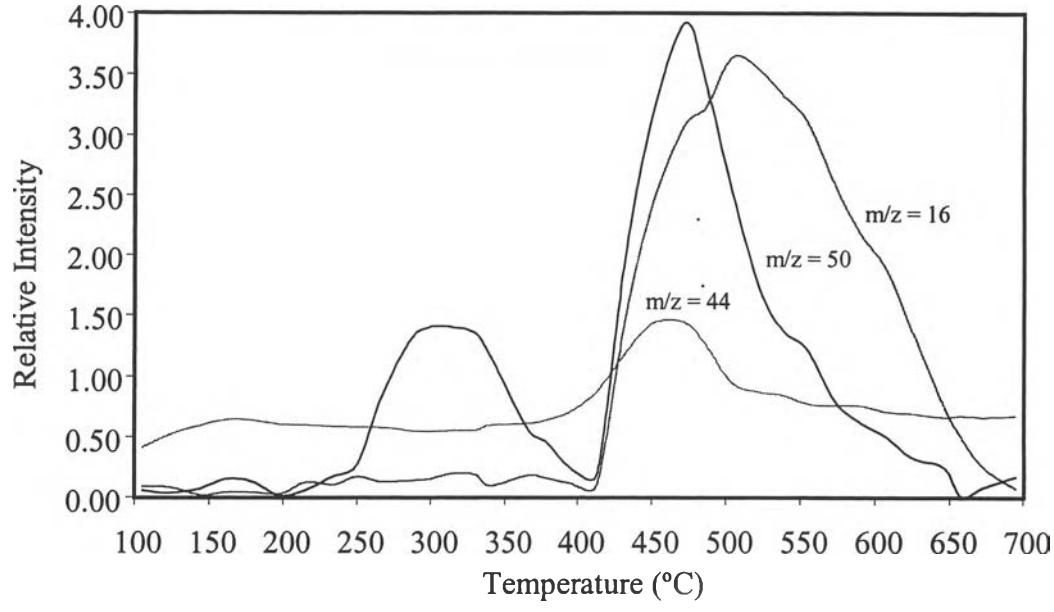

Figure 4.3.3 Mass spectra of products, m/z = 16, 44, and 50, from the pyrolysis of API separator sludge with $10°C \cdot min^{-1}$ heating rate.

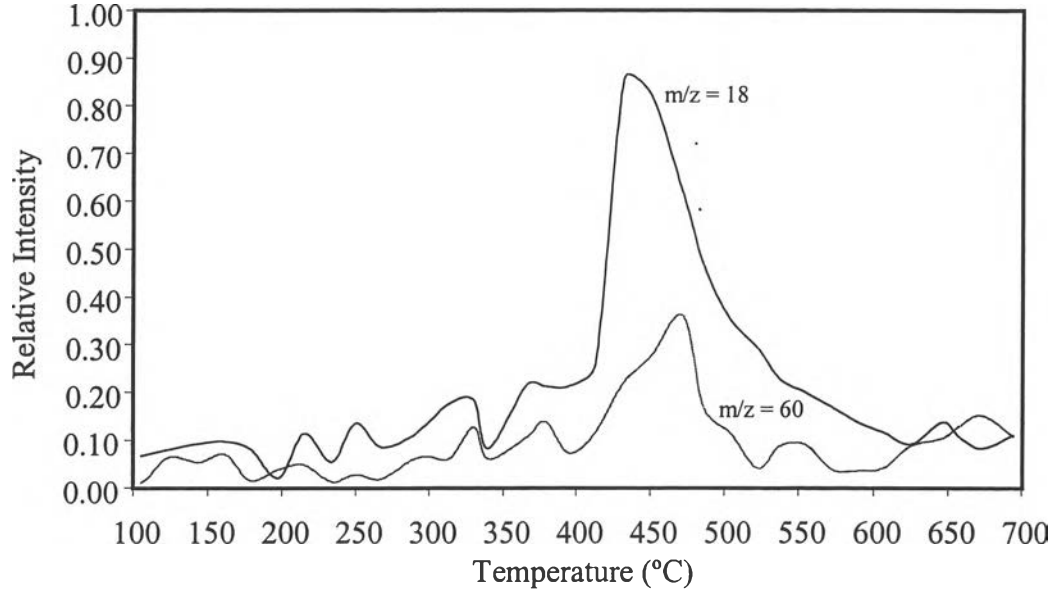

Figure 4.3.4 Mass spectra of products, m/z = 18 and 60, from the pyrolysis of API separator sludge with $10°C \cdot min^{-1}$ heating rate.

Approximately, 15 mg of the sample was subjected to a series of heating rates in the TGA. The temperature was ramped with the heating rate of $5°C \cdot min^{-1}$ from the room temperature to 200°C, where the sample was maintained for 20 min. Afterwards, the sample was cooled to 100°C and followed by heating up to 700°C with the same heating rate as shown in Figure 4.4.

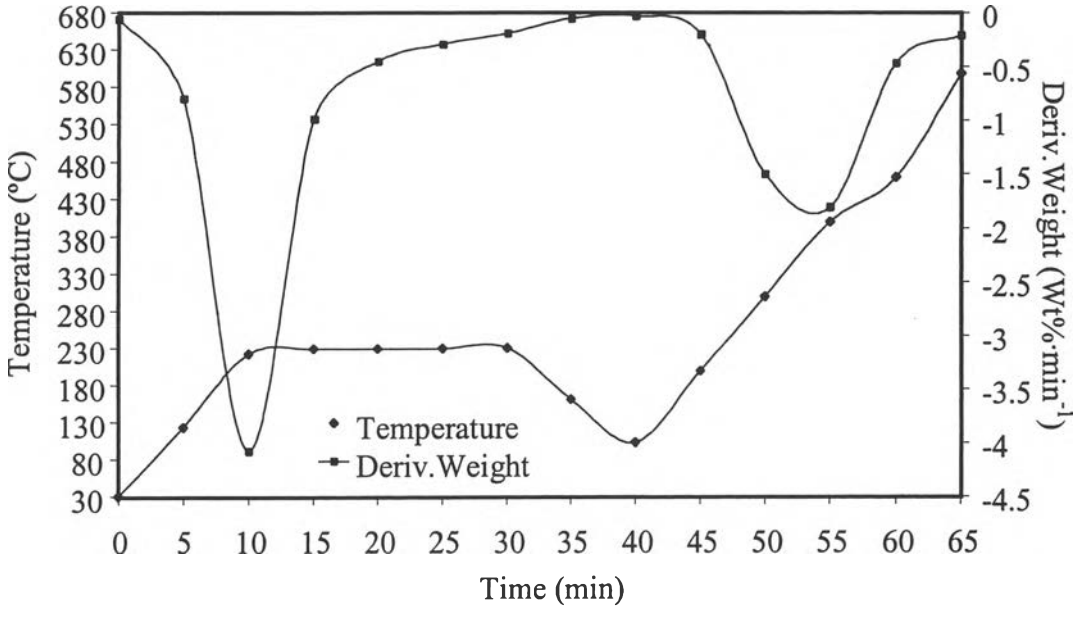

Figure 4.4 DTG and temperature profile to prove the volatilization of the thermal conversion of API separator sludge.

The main pyrolysis for the sludge takes place between 415 and 440°C depending on the heating rates. It was the same as reported for the pyrolysis of polyvinyl alcohol (Shie *et al.*, 2002), ligno-cellulosic and ebonite materials (Senneca *et al.*, 2002), and rubber waste (Lin *et al.*, 1996). The products from the main pyrolysis of this study were listed in Figures 4.3.1-4.3.4 and Table 4.4. Although the exact amount of each gas product were not the main objective of this work, hydrogen and acetylene seem to be the dominant products due to the pyrolysis of the sludge sample. This was different from the main products, carbon dioxide and carbon monoxide, from the pyrolysis of the industrial wastewater plants reported by Caballero *et al.* (1997).

If the weight loss at the low temperature were due to anything but volatilization, the same peak would be observed with the second heat up. As seen from the figure, the DTG curve indicated that the peak at the low temperature could not be observed at the second heat up. The only peak at the second heat up was ca. 400°C. Therefore, the weight loss at the low temperature was the result of volatilization. This was also confirmed by the MS results, which showed that no pyrolysis products occurred at this temperature range.

4.3 Mathematical Modeling

The concept of global reaction kinetic of thermal decomposition might be represented by the n^{th}-order reaction rate equation (Garcia *et al.*, 2001; Leung *et al.*, 1999; Liu *et al.*, 2002; Caballero *et al.*, 1995; Burnham and Braun, (1999); Guo *et al.*, 2001):

$$\frac{dx}{dt} = kf(x)^n, \tag{4.1}$$

where t is time used in pyrolytic process, n is reaction order; x is the weight loss fraction of reactive component,

$$x = \frac{w_i - w_o}{w_e - w_o}, \tag{4.2}$$

where w_i, w_o, and w_e mean mass percentage of sample at any time, the initial mass percentage of material, and the final mass percentage of the material, respectively. The reaction rate constant (k) can be described in the form of the Arrhenius equation:

$$k = A\exp\left(-\frac{E_a}{RT}\right), \tag{4.3}$$

where A is pre-exponential factor, R is the gas constant, E_a is activation energy and T is absolute temperature.

Following Coat and Redfern (1964), it was assumed that all experiments have no buoyancy and heat transfer effect. This lead to the ordinary differential equation describing the weight loss fraction of the sludge:

$$\frac{dx}{dT} = A\exp\left(-\frac{E_a}{RT}\right)[f(x)]^n \tag{4.4}$$

If the relationship of time (t) and increased temperature (T) is in the form of

$$T = \beta t + T_{ref}, \tag{4.5}$$

where T_{ref} is reference temperature and β is constant factor. Differentiating on both sides of Eq. (4.4) with respect to time gives $\frac{dT}{dt} = \beta$ or heating rate. Eq. (4.4) can be written as

$$\frac{dx}{dT} = \frac{A}{\beta}\exp\left(-\frac{E_a}{RT}\right)[f(x)]^n \tag{4.6}$$

By rearrangement and integrating equation (4.6), the integral equation is in the form of

$$\int_{T_0}^{T}\frac{dx}{[f(x)]^n} = \int_{T_0}^{T}\frac{A}{\beta}\exp\left(-\frac{E_a}{RT}\right)dT = \int_{T_0}^{T}\frac{k(T)}{\beta}\,dT \tag{4.7}$$

If the experiment runs at constant heating rate, equation (4.7) can be written as:

$$\int_{T_0}^{T}\frac{k(T)}{\beta} = \frac{1}{\beta}\int_{T_0}^{T}A\exp\left(-\frac{E_a}{RT}\right)dT \tag{4.8}$$

The right-hand side of equation (4.8) can not be integrated. To solve this problem, the approximation of exponential integral term is applied.

$$\int_{T_0}^{T} \frac{k(T)}{\beta} = \frac{ART^2}{\beta E_a}\left[1 - \frac{2RT}{E_a} + \ldots\right]\exp\left(-\frac{E_a}{RT}\right) \tag{4.9}$$

The left-hand side of equation (4.7) can be defined as

$$F(x) = \int_0^x \frac{dx}{[f(x)]^n} \tag{4.10}$$

Coupling equation (4.7), (4.9), and (4.10), hence

$$F(x) = \frac{ART^2}{\beta E_a}\left[1 - \frac{2RT}{E_a} + \ldots\right]\exp\left(-\frac{E_a}{RT}\right) \tag{4.11}$$

The independent pseudo bi-component model (Liu *et al.*, 2002) is applied here for the weight loss of the API separator sludge:

$$\frac{dx}{dT} = \begin{cases} \dfrac{dx_1}{dT} & w_{1o} < w_{1i} < w_{1e} \\ \dfrac{dx_2}{dT} & w_{1e} = w_{2o} < w_{2i} < w_{2e} \end{cases}, \tag{4.12}$$

where

$$\frac{dx_1}{dT} = \frac{A_i}{\beta}\exp\left(-\frac{E_{ai}}{RT}\right)[f(x)]^{n_1}, \tag{4.13}$$

$$\frac{dx_2}{dT} = \frac{A_2}{\beta}\exp\left(-\frac{E_{ai}}{RT}\right)[f(x)]^{n_2}, \tag{4.14}$$

and subscripts 1 and 2 correspond to the pseudo components 1 and 2, respectively. The various functional form of f (x) are presented in Table 4.5. In its commonly presumed form for solid-state reaction f (x) = (1-x).

Table 4.5 Commonly used functional forms of f (x) (Liu *et al.*, 2002; Conesa *et al.*, 2001)

Designation	f(x)	Description of reaction process
A2	$2(1-x)[-\ln(1-x)]^{1/2}$	Random nucleation, Avrami-Erofe'ev equation
A3	$3(1-x)[-\ln(1-x)]^{2/3}$	Random nucleation, Avrami-Erofe'ev equation
A4	$4(1-x)[-\ln(1-x)]^{3/4}$	Random nucleation, Avrami-Erofe'ev equation
D1	$1/2x$	One dimensional diffusion
D2	$[-\ln(1-x)^{1/3}]^{-1}$	Two-dimensional diffusion
D3	$3/2(1-x)^{2/3}[1-(1-x)^{1/3}]^{-1}$	Three-dimensional diffusion
D4	$3/2[(1-x)^{-1/3}-1]^{-1}$	Four-dimensional diffusion
F0	1	Zero-order
F1	1-x	First-order
F2	$(1-x)^2$	Second-order
F3	$(1-x)^3$	Third-order
R2	$2(1-x)^{1/2}$	Cylindrical phase boundary
R3	$3(1-x)^{2/3}$	Spherical phase boundary

To investigate our kinetic parameters, the details of calculation kinetic parameters were explained here. The experimental data of TGA curve were used to plot the DTG curves over all temperature range. Then, DTG curves were divided into two zones with two-temperature interval. For first zone, by taking natural logarithm both sides of equation (4.11), the equation was in the new form of:

$$\ln\left(\frac{F(x)}{T^2}\right)=\ln(S) - \frac{E_{ai}}{RT} \tag{4.15}$$

where

$$S= \frac{A_i R}{\beta E_{ai}}\left(1 - \frac{2RT}{E_{ai}}\right) \tag{4.16}$$

By varying the parameter n in equation (4.10) and plotting $\frac{1}{T}$ versus $\ln\left(\frac{F(x)}{T^2}\right)$, the curves obtained were in the linear curves as shown in Figure 4.5.1--4.5.6. Choose the best parameter n with give the most R^2 values. First of all the term $\frac{2RT}{E_{ai}}$ in equation (4.16) could be neglected because this term is less than 1. Activation energy (E_{ai}) and pre-exponential factor (A_i) for each section could then be calculated from the slope and y-intercept, respectively. By following this definition, the value of A_i (not defined) could be calculated from intercepting directly.

In order to obtain the corrected values of E_{ai} and A_i, linear correlation coefficients, R^2, received from the computer program were compared. If considered linear functions had a maximum value of correlation coefficients, the E_{ai} and A_i, then, were the most accuracy and can be accepted. To further obtain refined A_i and E_{ai}, the linear function calculated from equation (4.15) are used. For finding refined A_i, the y-axis intercept values were plotted to show the relationship between temperature and A_i. Now, the second term, $\frac{2RT}{E_{ai}}$, of Coat and Redfern model in equation (4.16) was used. Note that E_{ai} was not refined activation energy for each reaction step (1 and 2). Then, equation (4.16) was arranged and written in the new form:

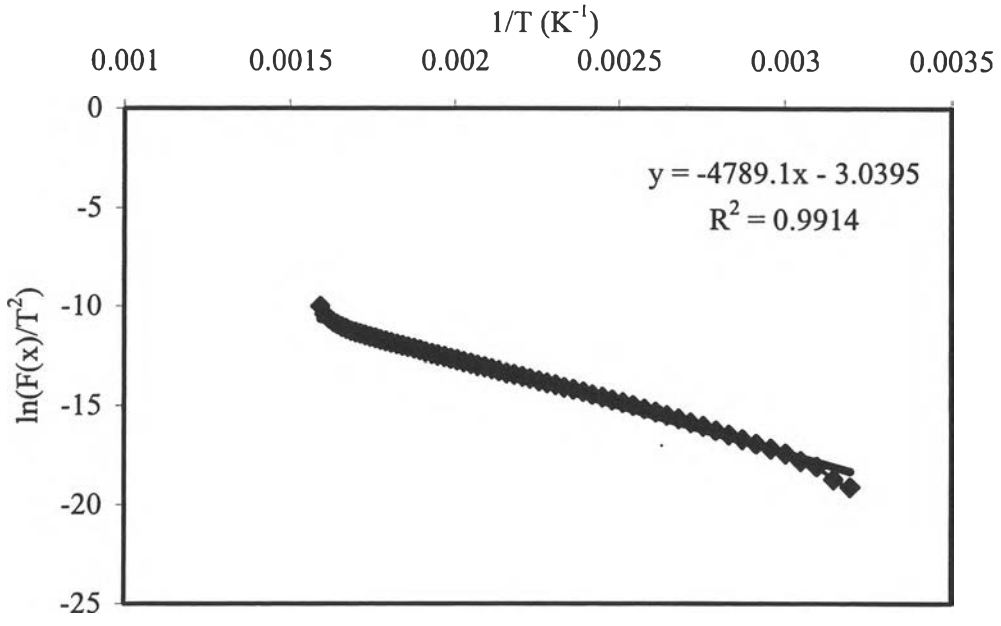

Figure 4.5.1 Relationship between $\ln\left(\frac{F(x)}{T^2}\right)$ and $\frac{1}{T}$ with equation and R^2 value, n = 1.5, of first reaction zone (30 to 360°C) for $5°C \cdot min^{-1}$ heating rate.

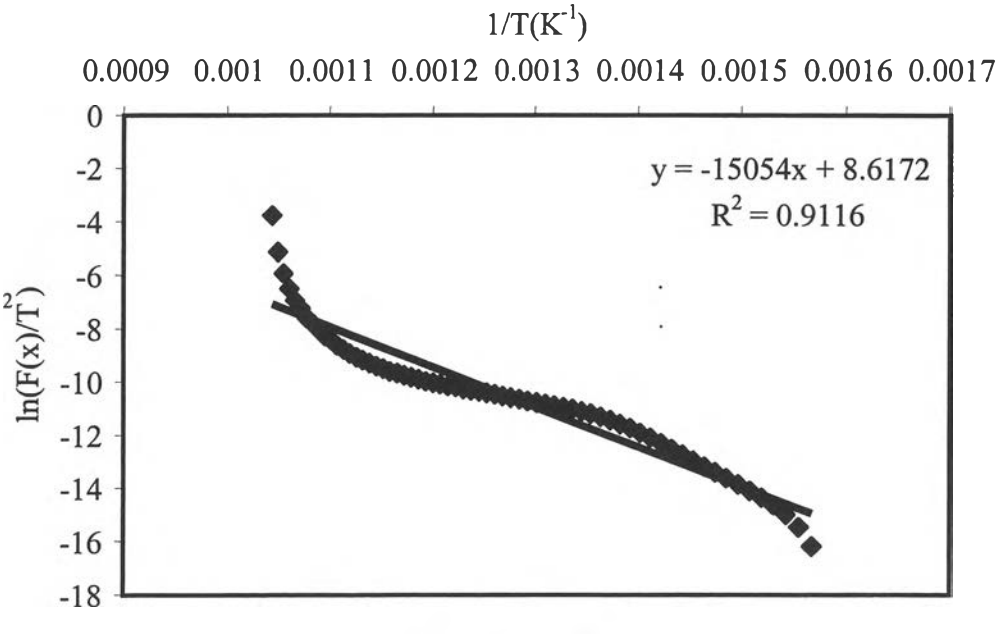

Figure 4.5.2 Relationship between $\ln\left(\frac{F(x)}{T^2}\right)$ and $\frac{1}{T}$ with equation and R^2 value, n = 3.0, of second reaction zone (360 to 700°C) for $5°C \cdot min^{-1}$ heating rate.

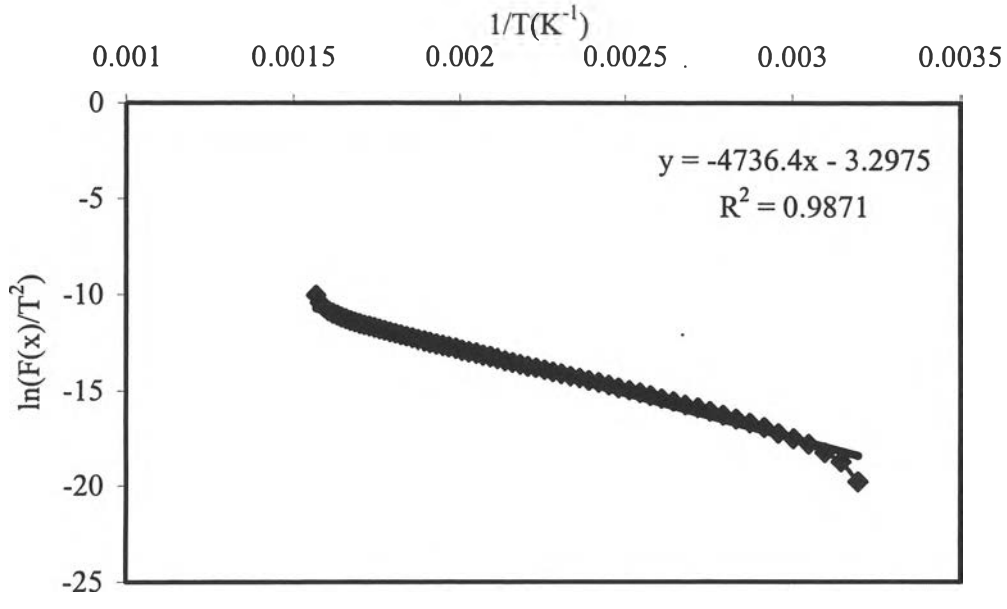

Figure 4.5.3 Relationship between $\ln\left(\frac{F(x)}{T^2}\right)$ and $\frac{1}{T}$ with equation and R^2 value, n = 1.5, of first reaction zone (30 to 370°C) for 10°C · min^{-1} heating rate.

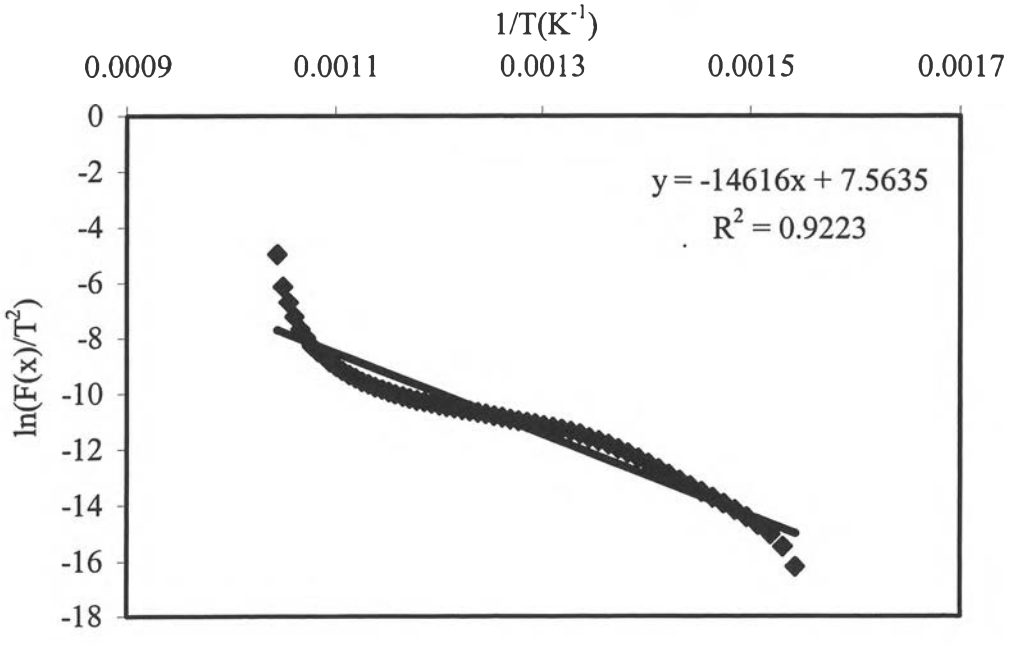

Figure 4.5.4 Relationship between $\ln\left(\frac{F(x)}{T^2}\right)$ and $\frac{1}{T}$ with equation and R^2 value, n = 2.8, of second reaction zone (370 to 700°C) for 10°C · min^{-1} heating rate.

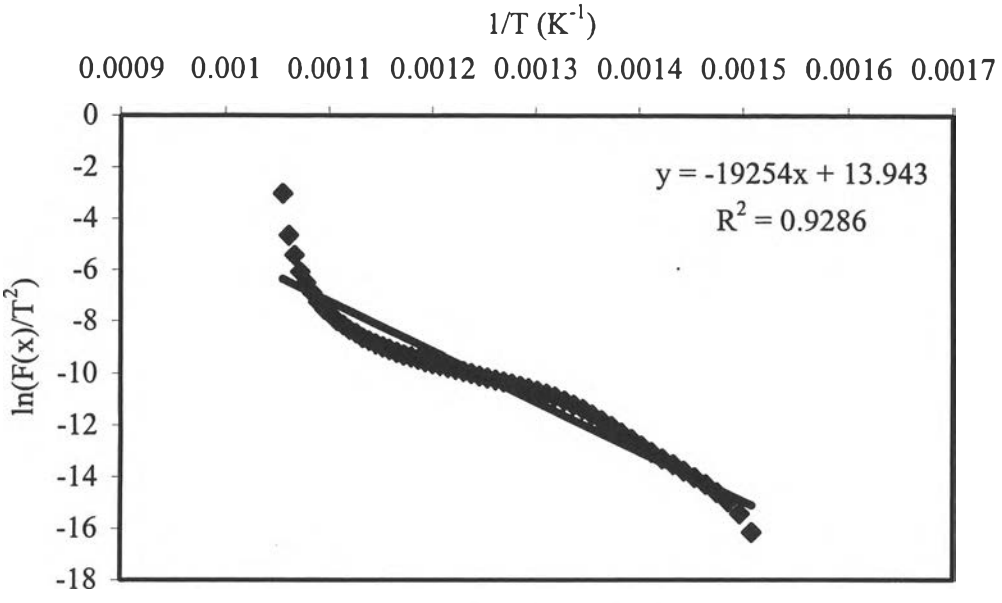

Figure 4.5.5 Relationship between $\ln\left(\frac{F(x)}{T^2}\right)$ and $\frac{1}{T}$ with equation and R^2 value, n = 1.3, of first reaction zone (30 to 385°C) for 20°C · min^{-1} heating rate.

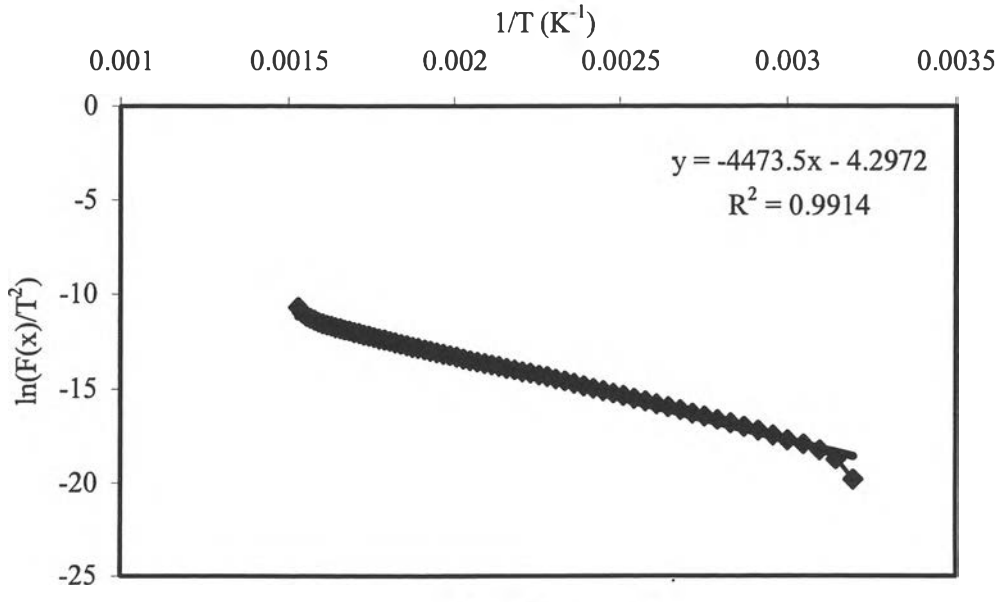

Figure 4.5.6 Relationship between $\ln\left(\frac{F(x)}{T^2}\right)$ and $\frac{1}{T}$ with equation and R^2 value, n = 3.1, of second reaction zone (385 to 700°C) for 20°C · min^{-1} heating rate.

$$A_i = \frac{\beta E_{ai} \exp(S)}{\left(1 - \frac{2RT}{E_{ai}}\right)} \qquad (4.17)$$

This equation could be calculated pre-exponential factor (A_i) at any temperature by using not refined activation energy.

In order to obtain the refined E_{ai}, first of all, we must know the activation energy for each section at all temperature range. The equation (4.15) was applied. From this equation, S-function was activation energy function so the equation (4.15) was so difficulty to solve the activation energy values for all heating rates reaction parts (first and second reaction), temperature and pre-exponential factors. The best way to do was rearrangement all variables from the right-hand side to the left-hand side and defined the new function, f (E_{ai}), as follow:

$$f(E_{ai}) = \ln\left(\frac{F(x)}{T^2}\right) - \ln(S) + \frac{E_{ai}}{RT} = 0 \qquad (4.18)$$

This equation required an initial guess of E_{ai} and iteration until the desired accuracy for E_{ai} at all over temperature range was achieved. To test the quality of proposed kinetic model, all kinetic parameter were substituted in equation (4.6) of each reaction part. Weight fraction of solid residue, then, was calculated from arrangement Coat and Redfern equation.

For reaction order, n, not equaled to 1, the weight faction equation was

$$x = 1 - \left[1 - (1-n)\frac{A_i RT^2}{\beta E_{ai}} \exp\left(-\frac{E_{ai}}{RT}\right)\left(1 - \frac{2RT}{E_{ai}}\right)\right]^{\frac{1}{1-n}} \qquad (4.19)$$

The model was fitted to the experimental data at each heating rate. Furthermore, the mean relative error of the fitting was calculated by Garcia *et al.* (2001):

$$\bar{\varepsilon}_r(\%) = \sqrt{\frac{\sum_{i=1}^{N}\left(\frac{w_{i,exp} - w_{i,cal}}{w_{i,exp}}\right)^2}{N}} \times 100, \qquad (4.20)$$

where N was the number of experimental data used in the fitting.

The kinetic parameters and mean relative errors of the fitting were summarized in Table 4.6.

Table 4.6 Kinetic parameters of the pseudo bi-component model and mean relative error for the API separator sludge pyrolysis at 5, 10, and 20°C · min^{-1}

Heating rate (°C · min^{-1})	Reaction step	Reaction order (n)	E_{ai} (kJ · mol^{-1})	ln(A) (min^{-1})	Mean relative error (%)
5	First	1.5	39.824	11.283	1.36
	Second	3.0	125.150	23.850	
10	First	1.5	39.386	11.038	1.42
	Second	2.8	128.300	23.850	
20	First	1.3	37.201	10.036	1.20
	Second	3.1	160.070	29.086	

The results show that the apparent reaction orders were approximately 1.5 and 3.0 for the first and second reaction step for the three heating rates. Similarly, there were no significant difference in the activation energy and pre-exponential factors for the 5 and 10°C · min^{-1} heating rates but a slightly higher in both values could be observed with the 20°C · min^{-1} heating rate. The results were consistent with the experimental data from TGA. The activation energy indicated that the first reaction corresponding to the weight loss at the low temperatures taked place much more easily compared to the second reaction. The relationship between pre-exponential factor (A) and absolute temperature (T) was also shown in Table 4.7 for each heating rate. The mean relative error from the fitting was less than 1.50 % for all heating rates. Figure 4.6.1–4.6.9 showed the fitting results.

Table 4.7 The relationship between pre-exponential factor (A) and temperature (T) in unit Kelvin of 5, 10, and 20°C · min^{-1} heating rates

Heating rate (°C · min^{-1})	Reaction step	Relation function	Temperature Range (K)
5	First	$A(T) = 0.0215 \cdot T^2 + 21.109 \cdot T + 64597$	313-628
	Second	$A(T) = 571.59 \cdot T^2 + 3x10^6 \cdot T + 2x\ 10^{10}$	638-953
10	First	$A(T) = 0.0174 \cdot T^2 + 16.344 \cdot T + 50302$	313-638
	Second	$A(T) = 553.22 \cdot T^2 + 3 \times 10^6 \cdot T + 2 \times 10^{10}$	648-958
20	First	$A(T) = 0.0075 \cdot T^2 + 5.8421 \cdot T + 18185$	313-653
	Second	$A(T) = 89892 \cdot T^2 + 6 \times 10^8 \cdot T + 6 \times 10^{12}$	663-945

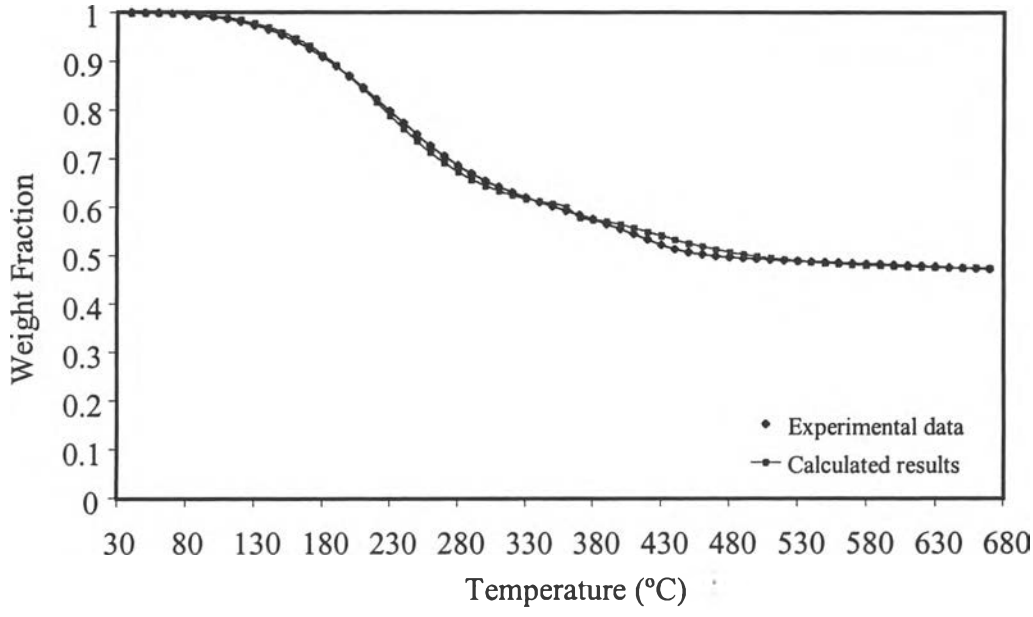

Figure 4.6.1 Comparison of TGA curves between experimental data and calculated results from the pseudo bi-component model at the heating rate of $5°C \cdot min^{-1}$.

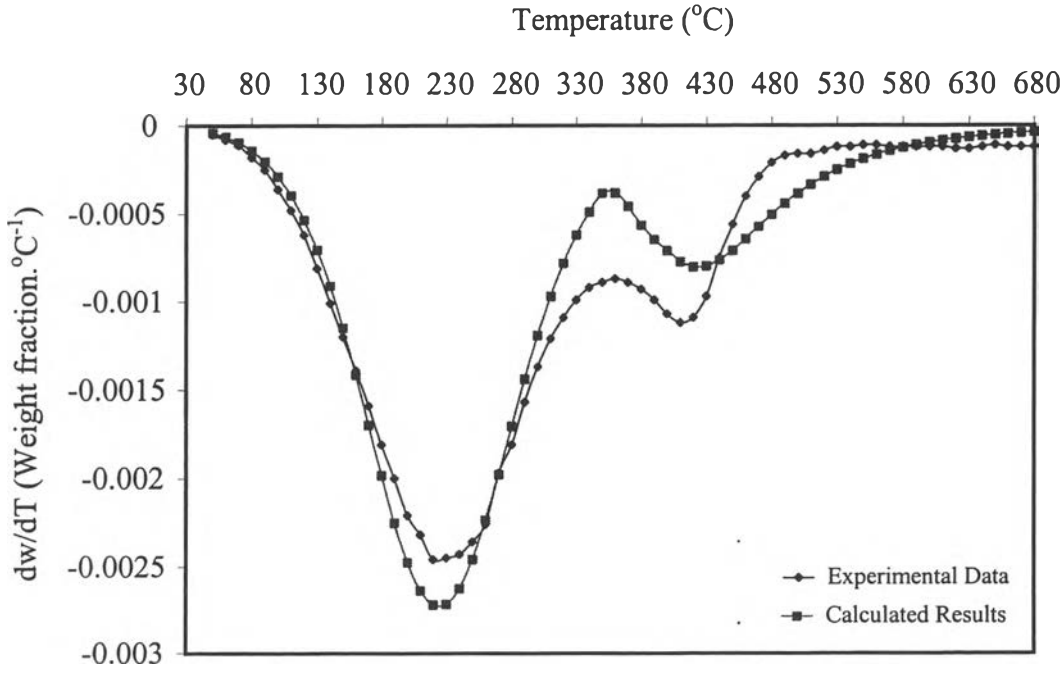

Figure 4.6.2 Comparison of DTG curves between experimental and calculated results from the pseudo bi-component model at the heating rate of $5°C \cdot min^{-1}$.

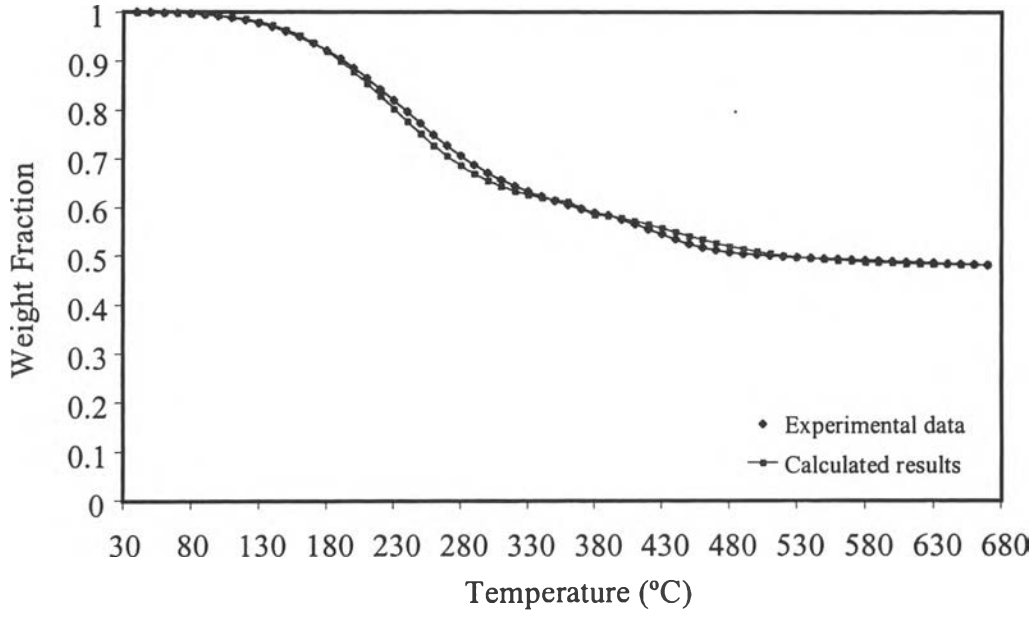

Figure 4.6.3 Comparison of TGA curves between experimental data and calculated results from the pseudo bi-component model at the heating rate of $10°C \cdot min^{-1}$.

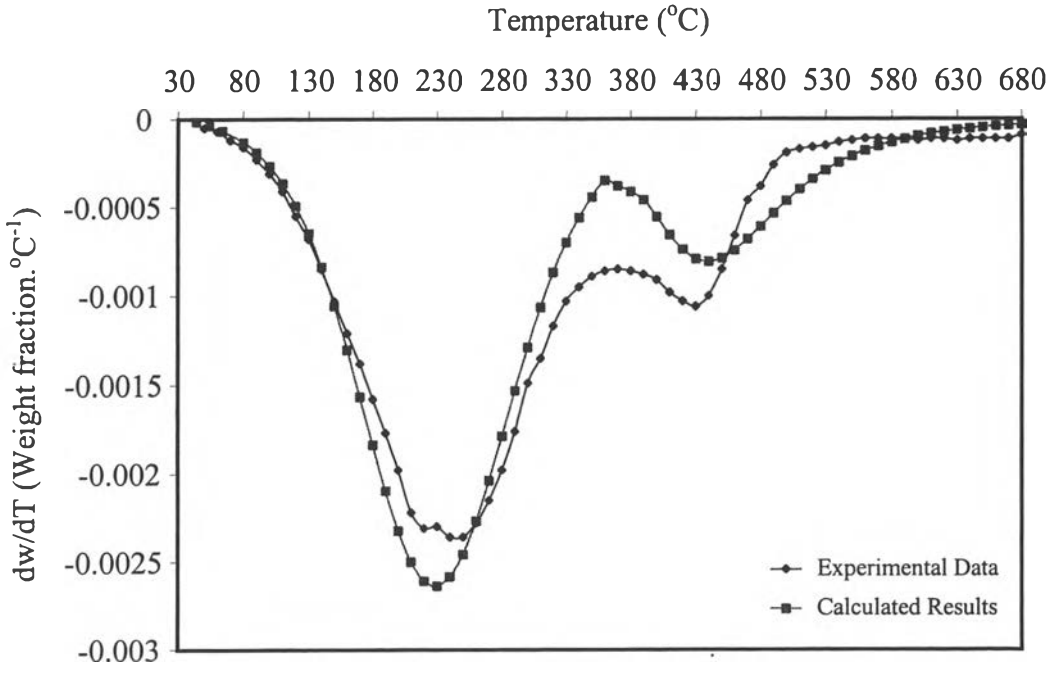

Figure 4.6.4 Comparison of DTG curves between experimental and calculated results from the pseudo bi-component model at the heating rate of $10°C \cdot min^{-1}$.

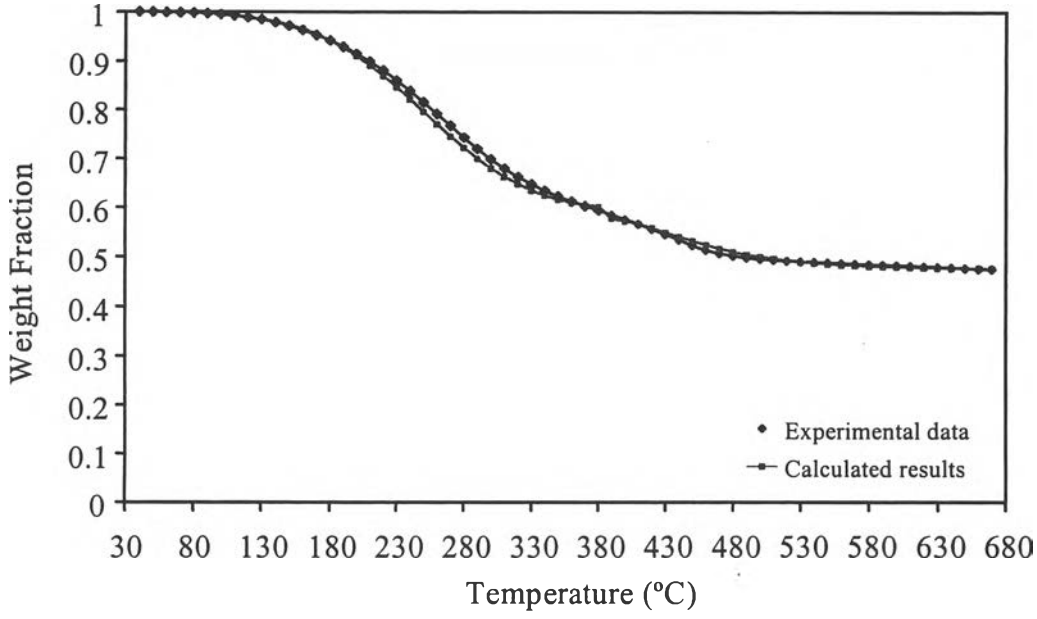

Figure 4.6.5 Comparison of TGA curves between experimental data and calculated results from the pseudo bi-component model at the heating rate of $20°C \cdot min^{-1}$.

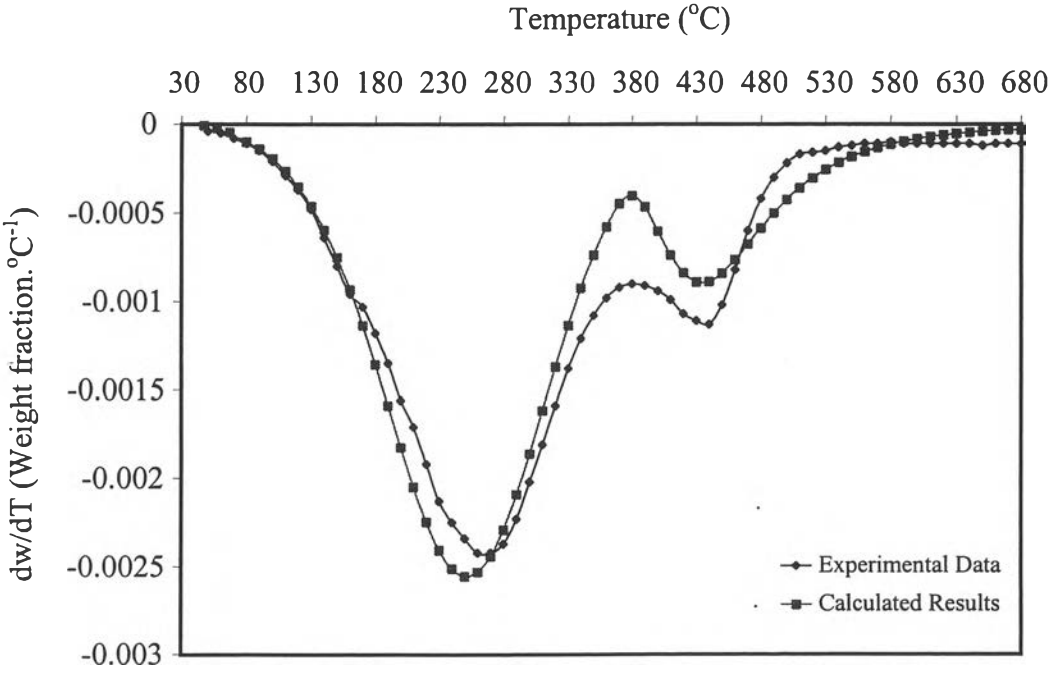

Figure 4.6.6 Comparison of DTG curves between experimental and calculated results from the pseudo bi-component model at the heating rate of $20°C \cdot min^{-1}$.

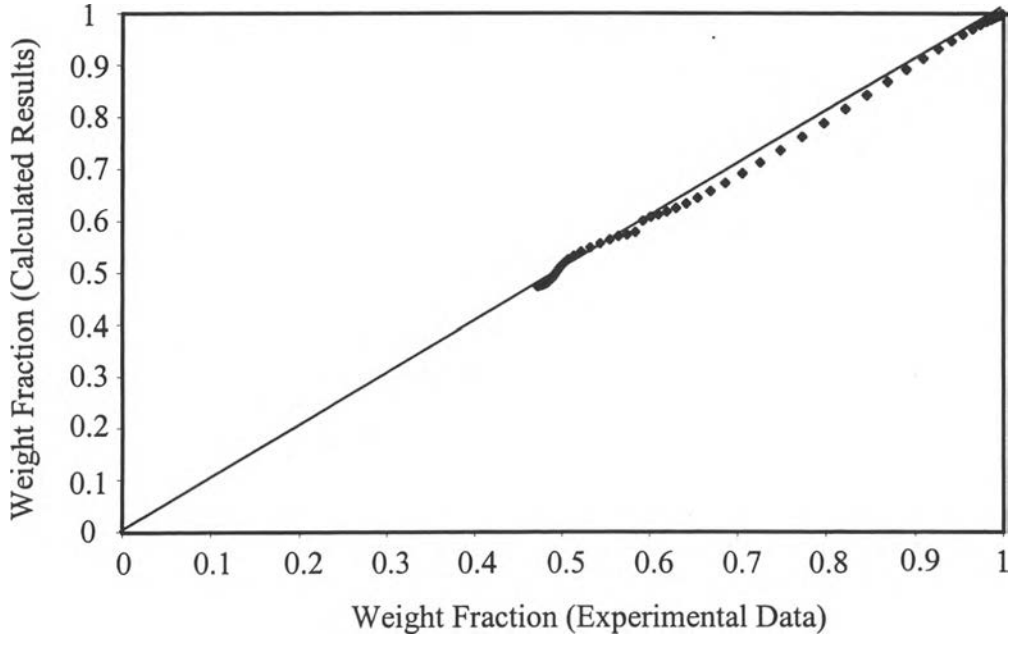

Figure 4.6.7 Comparison of weight fraction between experimental and calculated results from the pseudo bi-component model at the heating rate of $5°C \cdot min^{-1}$.

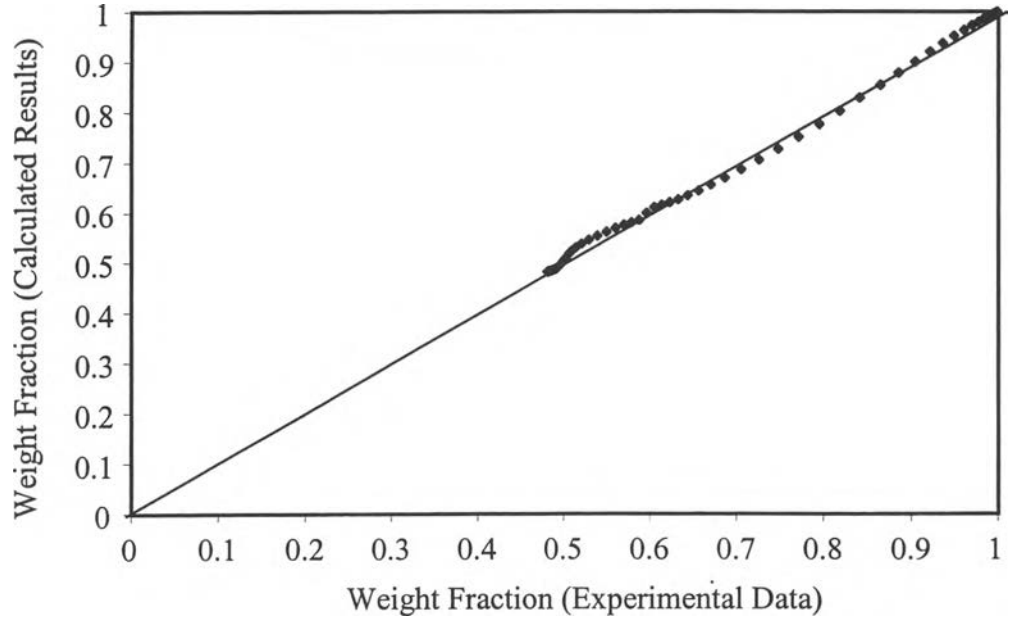

Figure 4.6.8 Comparison of weight fraction between experimental and calculated results from the pseudo bi-component model at the heating rate of $10°C \cdot min^{-1}$.

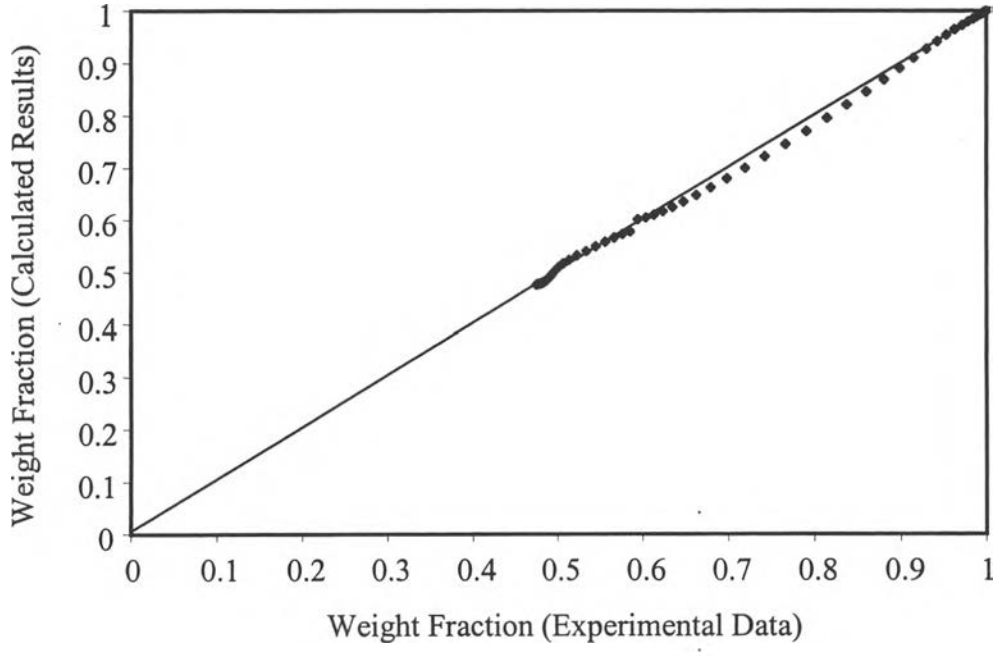

Figure 4.6.9 Comparison of weight fraction between experimental and calculated results from the pseudo bi-component model at the heating rate of $20°C \cdot min^{-1}$.